# Mechanism of negative membrane curvature generation by I-BAR domains

Binod Nepal<sup>1</sup>, Aliasghar Sepehri<sup>1</sup>, Themis Lazaridis<sup>1,2,3\*</sup>

<sup>1</sup>Department of Chemistry, City College of New York, New York, NY 10031, USA

<sup>2</sup>Graduate Programs in Chemistry, Biochemistry, and Physics, The Graduate Center,

City University of New York, New York, New York, USA

<sup>3</sup>Lead Contact

\* Correspondence: tlazaridis@ccny.cuny.edu

#### **SUMMARY**

The membrane sculpting ability of BAR domains has been attributed to the intrinsic curvature of their banana-shaped dimeric structure. However, there is often a mismatch between this intrinsic curvature and the diameter of the membrane tubules generated. I-BAR domains are especially mysterious since they are almost flat but generate high negative membrane curvature. Here, we use atomistic implicit-solvent computer modeling to show that the membrane bending of the IRSp53 I-BAR domain is dictated by its higher oligomeric structure, whose curvature is completely unrelated to the intrinsic curvature of the dimer. Two other I-BARs give similar results, whereas a flat F-BAR sheet develops a concave membrane binding interface, consistent with its observed positive membrane curvature generation. Laterally interacting helical spirals of I-BAR dimers on tube interiors are stable and have an enhanced binding energy that is sufficient for membrane bending to experimentally observed tubule diameters at a reasonable surface density.

#### INTRODUCTION

Remodeling of the cell membrane is involved in key biological processes such as endocytosis, viral budding, and membrane fission/fusion (Besterman and Low, 1983; Chen and Scheller, 2001; Chernomordik and Kozlov, 2008; Chlanda et al., 2017; Eitzen, 2003; Kaksonen and Roux, 2018; Suetsugu, 2010; Wu et al., 2014). This is usually accomplished by specialized proteins that can sense and generate membrane curvature. One important class of such proteins is the BAR domain family, consisting of crescent-shaped dimers and classified into three groups. Classical BAR/N-BAR domains generate or stabilize high, positive membrane curvature with intrinsic radius from 5.5 to 40 nm (Masuda et al., 2006; Pang et al.; Peter et al., 2004) (Zhu et al., 2007). The N-BAR domains contain an additional N-terminal amphipathic helix (H0 helix), which can assist in membrane binding and/or curvature generation. F-BAR domains tend to generate or stabilize lower positive membrane curvature than classical BAR domains with tubule diameters ranging from 64-113 nm (Frost et al., 2008). Finally, inverse BAR (I-BAR) domains stabilize or generate negative membrane curvature. These have a positively charged surface that is slightly convex in the crystal structures, which is thought to help them bind efficiently on the concave surface of the membrane. I-BAR domains are present in several proteins, including insulin receptor substrate P53 (IRSp53), insulin receptor tyrosine kinase receptor (IRTKS), missing-inmetastasis (MIM) and actin-bundling protein with BAIAP2 homology (ABBA), IRSp53 and IRTKS I-BAR domains bind to the membrane mainly through electrostatic interactions but MIM and ABBA also insert their N-terminal helix into the membrane interior (Saarikangas et al., 2009).

There is evidence that generation of global membrane curvature requires assemblies of BAR proteins. For example, cryo-EM studies found that F-BAR domains polymerize into helical coats, stabilized by both tip-to-tip and lateral interactions (Frost *et al.*, 2008). It is possible that I-BAR proteins behave similarly but evidence for this is currently lacking. The binding of these proteins to PI(4,5)P2 further complicates the mechanism, as I-BAR domains were found to cause PI(4,5)P2 clustering (Linkner et al., 2014; Saarikangas et al., 2010). Asymmetric distribution of PI(4,5)P2 promotes membrane curvature generation even without peptides (Shukla et al., 2019) or just with simple cations like Ca<sup>2+</sup> (Graber et al., 2017). Proteins that generate negative membrane curvature bind to the inner leaflet of tubules, and this makes them harder to study. Specialized techniques have been developed for negative curvature sensing peptides in the last five years. For example, pulling tubes from a GUV with encapsulated peptides provided a way to determine the preference of the IRSp53 I-BAR domain for ~18 nm radius (Prévost et al., 2015). More recently, a novel method utilizing protein sorting on tubular filopodia of varying diameter showed preferential binding to 25-nm and 19-nm radii for MIM I-BAR and IRSp53, respectively (Breuer et al., 2019).

Computer simulations could provide insights but are limited by the system size and computational resources. Few studies have appeared on I-BAR domains. All-atom simulations usually consider one dimer on the membrane surface for a short amount of time (Levtsova et al., 2011; Takemura et al., 2017), while coarse-grained simulations can handle large systems, at the cost of lower accuracy(Jarin et al., 2021; Jarin et al., 2019). All-atom molecular dynamics (MD) simulation showed that about 30 salt bridges are formed between I-BAR and membrane head groups, especially DOPS, whose density was enriched near the protein (Takemura et al., 2017). Kinks in the membrane appeared at the tips of the IBAR domain, which were interpreted as negative curvature. A coarse-grained MD simulation showed the generation of negative curvature but shallower than that generated experimentally (Levtsova et al., 2011). Moreover, the peptide was not binding through its convex surface and, depending on the binding orientation, it also generated positive membrane curvature. Another coarse-grained study showed similar I-BAR mediated PI(4,5)P2 clustering; no membrane deformation was seen but PIP2 was observed to prefer negative curvatures in precurved membranes (Lin et al., 2018). A more recent coarsegrained study found that the peptide tends to orient along the axis of the 20 nm radius tube (Jarin et al., 2019). This result is puzzling, considering the curvature preference for 20 nm tubes. If individual I-BAR domains do not prefer to be aligned with the curvature, then how can they sense or stabilize it?

One possible explanation is that I-BAR domains form higher oligomers that are responsible for curvature sensing and generation. If so, how does each I-BAR dimer arrange to form higher oligomers? IRSP53 I-BAR generates tubules with average diameter of about 43-nm (Saarikangas *et al.*, 2009). What dictates this? In the present work we sought answers to these questions using an implicit membrane model for curved membranes (Nepal et al., 2018). This approach represents proteins in atomistic detail while water and lipids are treated as a continuum. In aqueous solution, the proteins interact via a well-established implicit water model (Lazaridis and Karplus, 1999). The membranes are represented as a hydrophobic slab of flat, spherical, or cylindrical shape with smooth transition between the nonpolar interior and the aqueous exterior (Lazaridis, 2003). The surface charge of the membrane, due to anionic lipids, is assumed to be uniform and is treated using the Gouy-Chapman theory in the case of flat shapes (Lazaridis, 2005) or approximate analytical solutions to the nonlinear Poisson-Boltzmann equation in the case of curved shapes (Nepal et al., 2020). We recently used the same approach to study the interaction of the ESCRT III subunit snf7 with flat and curved membranes (Nepal *et al.*, 2020).

## **RESULTS**

## Binding orientation, energetics and curvature sensitivity of the dimer

The IRSp53 IBAR domain is an elongated dimer with a slightly convex membrane-binding surface in the crystal structures (Millard et al., 2005; Suetsugu et al., 2006) (Fig. 1a). To determine the preferred membrane-binding orientation in our model, we conducted four simulations with the protein (PDB ID 1Y2O) placed with its long axis parallel to a 30% anionic flat implicit membrane but with different rotation angles around its axis. In all cases the dimer bound to the membrane in a well-defined configuration (Fig. 1a) which is identical to that presumed in the crystal structures and found in all-atom simulations (Takemura *et al.*, 2017). The membrane-binding interface contains a large number of positively charged residues making varying contributions to binding (Table S1). Consistent with previous simulations and mutation studies (Levtsova *et al.*, 2011; Takemura *et al.*, 2017), the residues near the end regions of the dimer interact more strongly with the membrane than those in the middle region. Surprisingly, due to the middle region, the binding interface appears not convex as in the crystal structure but concave Fig. 1a).

The dimer binds similarly onto the interior of a 30-nm vesicle (Fig. 1c). The same positively charged residues contribute to membrane binding but the fit appears improved. In the binding configuration of the dimer on the exterior of a 30-nm vesicle (Fig. 1b) the middle region positive residues bind somewhat better, but there is significant loss of interactions in the arms. It seems that what matters for curvature sensing is not the curvature of the entire surface but only that of the two arms alone. The angle between the two arms (Fig. 1c) is flatter on the flat membrane compared to the interior of the spherical surface (Fig. S1).

The orientational preference of the I-BAR dimer on cylindrical membrane tubes is presented in Table S2. In narrow tubes, inside or outside, the dimer tends to orient parallel to the tube axis, in agreement with recent coarse-grained simulations<sup>23</sup>. On the larger tubes this orientational preference persists only for the tube exterior, indicating that I-BAR dislikes especially a convex surface. The binding energies of the IRSP53 I-BAR dimer on 30% anionic spherical and cylindrical membrane surfaces are shown in Table 1. We note that the magnitude of the calculated energies is similar to the -8.6 kcal/mol obtained by all-atom umbrella sampling calculations in a membrane containing 11% PS lipids (Takemura *et al.*, 2017). Binding energies on the interior spherical surface and on both cylindrical surfaces do not change much with curvature (the difference is within 0.3 kcal/mol). The latter is due to the preferred parallel orientation of the dimer to the tube axis. Only the exterior spherical surface is clearly less favorable at high curvature. Comparing the interior cylindrical and spherical surfaces, the cylindrical surface is slightly preferred, especially at higher curvature.

The curvature sensitivities of the dimer were also determined at different anionic fractions (Table 1). At 30% anionic fraction, there is only a slight distinction between high curvature and the flat membrane surface. At higher anionic fractions, which could mimic the effect of anionic lipid clustering, binding energy is maximal at 20 nm radius and minimal on the flat surface. The

curvature sensitivity parameter  $\alpha$  (defined in Methods) increases significantly on increasing anionic fraction. The ratio of the dissociation constants for 20 nm radius to flat membrane increases from 1 to 3 to 6 on moving from anionic fraction 30% to 50% to 75%. Since I-BAR dimers align with the tube axis, the observed curvature sensitivity is attributed to the stronger electrostatic interaction in the narrow tubes. The sorting ratio between the planar membrane and the 20-nm radius tubular membrane (Table S3) is 1.8 at 30% anionic membrane and increases to 6.4 upon increasing anionic percentage to 75%. A statistical analysis of these energy differences is shown in Table S4.

**Figure 1. Binding configuration of the dimer after 20 ns simulation.** (A) Flat membrane surface (B) Outside a spherical surface of radius 30 nm (C) Inside a spherical surface of radius 30 nm. The positively charged residues are shown in stick model. Shown is one of four independent trials, which give very similar results.  $\theta$  is the angle between the axes of the helices defined by residues 121-147.

#### Simulations of I-BAR self-assembly on a flat membrane surface

To identify possible oligomeric structures that might be responsible for generating or stabilizing tubular membranes, 2-20 I-BAR dimers were arranged on a rectangular lattice bound on a flat membrane surface at a distance of 5 to 40 nm from each other and were simulated without any bias (other than a loose restraint for the proteins to stay within a certain area). Four independent runs with two dimers resulted in mostly lateral interactions having various alignments and stabilized by salt bridges. This is expected due to the presence of an almost uniform distribution of the positively and negatively charged residues throughout the length of the dimer (Fig. S2). Lateral interactions (Fig. 2b and 2c) were more probable than end-to-end interactions (Fig. 2d). Furthermore, the end-to-end interaction of just two dimers was not stable and eventually resulted in a laterally interacting dimer. When four dimers were simulated on the flat membrane surface, three of them came together and formed a laterally overlapping higher oligomer (Fig. 2e). In further simulations of 6, 8, 9 and 20 dimers on a flat membrane both lateral and end-to-end interactions were encountered, but lateral interactions were more pronounced (e.g. Fig. S3 for 20 dimers). The lateral mode of oligomerization observed in Fig. 2b is very similar to that observed in the crystal structure (PDB id 1Y2O) (Millard et al., 2005) with a small difference in register (using Scheme S1 in SI, the crystal has  $\theta$ =29° and d2=76 Å, whereas Fig. 2b has  $\theta$ =33° and d2=62 Å).

Simulations of multiple I-BAR dimers were also carried out on the interior surface of a tubular membrane of 20-nm radius starting parallel or perpendicular to the tube axis. Again, the dimers interacted with each other both laterally and end-to-end. Most of the dimers tended to orient parallel to the tube axis. Hence, increasing the protein concentration to  $\sim$ 544 dimers/ $\mu$ m² does not lead to a preference for perpendicular orientation relative to the tube axis.

Table 1. Binding energies of I-BAR dimer on cylindrical and spherical lipid membranes of different radius and anionic fraction. The curvature sensitivity parameter  $\alpha$  is determined from the data for radii 20 nm to 50 nm. Values in kcal/mol.

sphere						£1 = 4	α
	10nm	20nm	30nm	40nm	50nm	flat	
Inside (30%)	_a _	-7.2±0.3	-7.3±0.3	-7.2±0.2	-7.6±0.3		
Outside (30%	-4.8±0.4	-5.5±0.5	-6.4±0.5	-7.2±0.5	-6.8±0.6		
	cylinder						
	10nm	20nm	30nm	40nm	50nm		
Inside (30%)	-7.6±0.1	-7.6±0.4	-7.4±0.4	-7.3±0.5	-7.4±0.1	-7.3±0.5	0.4±0.2
Inside (50%)	-11.0±0.1	-11.2±0.4	-11.2±0.4	-10.8±0.1	-10.6±0.9	-10.6±0.1	1.2±0.4
Inside (75%)	-13.6±0.1	-14.1±0.5	-14.0±0.2	-13.6±0.4	-13.5±0.3	-13.0±0.5	1.3±0.2
Outside (30%)	-6.8±0.3	-7.3±0.3	-7.5±0.1	-7.2±0.2	-7.1±0.6		

a. The dimer is too long to fit inside a 10-nm sphere.

#### Simulation of a chain and a sheet of dimers

Using the packing observed in the crystal structure we generated a linear chain of dimers (Fig. 3a) and simulated it in implicit water and on a flat membrane surface. In water the chain bent into a spiral shape with radius close to 20 nm (Fig. 3b). Importantly, the membrane binding interface lies on the outer surface of the spiral, indicating that the spiral would readily bind to a concave surface. Chains with different lateral alignments between the dimers all gave a similar spiral structure, showing that this result is robust with respect to oligomerization details. On the flat implicit membrane surface the simulation resulted in a 2-dimensional bent structure (Fig. 3c).

Figure 2. Configurations from self-assembly simulations of two or four I-BAR dimers on a flat membrane. (A) Initial configuration of two dimers. (B,C,D) Final configurations two dimers in different simulations. (E) Trimeric oligomer obtained from the free simulation of four dimers. Top view is shown in all figures.

**Figure 3. Configurations of a chain of I-BAR dimers.** (A) Initial arrangement of a chain of dimers based on the crystal structure. (B) Final configuration obtained after simulation in implicit water. (C) Final configuration obtained from the simulation on a flat membrane surface (view from above).

Similarly, a planar I-BAR sheet was constructed containing both lateral and end-to-end interactions (Fig. 4a) and was simulated in implicit water (for construction details of this and other oligomers see SI). The sheet rapidly turned into a tubular structure (Fig. 4b,c) whose membrane binding interface is on the outside, suitable for fitting into the interior of an anionic tubular membrane. Importantly, the sheet bent along the direction of the lateral overlap of the dimers, indicating that the bent structure of the I-BAR oligomer arises from the lateral interactions. The obtained structure had a radius of ~13 nm, slightly lower than the preferred curvature determined by experiment (Saarikangas *et al.*, 2009).

As a control, sheets of MIM I-BAR (PDB ID 2D1L) and I-BARa (PDB ID 4NQI) were also simulated in the aqueous phase. Both curved in such a way that the membrane binding surface lay on their convex surface. Interestingly, the curvature developed was smaller than that of

IRSP53 I-BAR, consistent with the experimental finding that MIM I-BAR generates larger size tubules than the IRSP53 I-BAR (Saarikangas *et al.*, 2009). Using the same protocol, an F-BAR sheet in aqueous solution (PDB ID 2V0O) developed a curvature with the membrane binding interface on its concave surface, consistent with positive curvature generating behavior. The structures are shown in Fig. S4-S6.

**Figure 4. Configurations of a sheet of I-BAR dimers.** (A) Initial structure of the planar sheet. (B,C) Final structure after simulation in implicit water, side view (B) and view along cylindrical axis (C).

# Simulations of preformed spirals inside a membrane tube

One of the important unresolved questions for I-BAR domains is how they arrange themselves inside membrane tubes. If they behave like other BAR domains, they should also form helical oligomeric structures. It is very difficult to obtain such structures from free simulations of multiple BAR dimers in a reasonable time. Thus, we constructed two types of spirals, with lateral interaction and end-to-end interaction (for construction details see Methods). The helical spiral consisting of lateral interactions is highly stable inside membrane tubes with 20 nm and 40 nm radii (Fig. 5 and S7). The spiral with only end-to-end interactions appeared highly flexible and did not have a definite shape inside the membrane tube (Fig. S8). We also constructed spirals with a combination of lateral and end-to-end interactions where the two helical filaments with end-to-end interactions are laterally overlapping. To design such spirals, the octameric unit (Fig. 6) that was obtained from the free assembly simulations was replicated. The designed spirals with radii 20 nm and 40 nm (Fig. S9) appear rigid and stable throughout the simulations. In both, only the pitch of the helical structure changed to match its curvature preference. In the 40-nm tube the spiral continuously decreases its pitch indicating it prefers a higher curvature. In this oligomeric structure, the orientational preference of individual dimers is satisfied, as they tend to remain parallel to the tube axis, especially inside the 20 nm tube.

Next, linear filaments were constructed with end-to-end interaction between the individual dimers (Fig. 7). The filaments were simulated on the flat membrane surface as well as on the interior of the membrane tube. In both simulations, the filaments failed to give a curved shape. Based on these results we propose that the lateral interaction between the dimers is responsible for negative curvature generation and stabilization.

Figure 5. Final configuration of the pre-constructed spiral after 20 ns simulation in the interior of a 20-nm cylindrical tube. The initial and final pitch of the helix is 110 nm and 107 nm, respectively.

Figure 6. Structure of tetramer of dimers obtained from the free simulation of multiple dimers on the flat membrane surface.

Figure 7. Linear filament designed by laterally overlapping two filaments with end-to-end interactions between the dimers.

# Binding energetics of low and high oligomers

The curvature sensitivity of a dimer of dimers (Fig. 2c) was examined on the interior of a 50% anionic tubular membrane. The binding energy (Table 2) is minimal at the flat membrane surface and increases gradually up to 10-20 nm, where the intrinsic curvature of the dimer of dimers is reached. The curvature sensitivity parameter  $\alpha$  obtained from the 20 nm to 50 nm data is 2.0, almost twice that for a single dimer on the same membrane. This suggests that the dimer of dimers tends to have a curved shape and is rigid enough to enhance curvature sensitivity.

The binding energetics of the filaments (constructed with lateral interactions) on the flat membrane and the interior of cylindrical membranes with anionic fraction 50% are also presented in Table 2. Binding energies are most favorable for the cylindrical spiral with radius 20 nm and least favorable for the filament on the flat membrane. This is consistent with the generation of smaller-size tubules. The sorting ratio between the flat and 20-nm cylindrical membrane, calculated from the average binding energy of the dimer to the membrane, is ~25.

Table 2. Binding energy per dimer in a dimer of dimers and filamentous I-BAR on a 50% anionic membrane. Averages were calculated from three trials and the last 10 ns of a 20-ns simulation. Values in kcal/mol.

Radius	10nm	20nm	30nm	40nm	50nm	Flat	α	Sorting Ratio (S)
Dimer of dimers	-10.3±0.2	-10.3±0.3	-9.8±0.3	-9.5±0.2	-9.2±0.5	-9.0±0.3	2.0	6.6
Filame- ntous <sup>a</sup>		-11.3±0.2		-10.2±0.2		-9.4±0.2	1.63	25.0

<sup>&</sup>lt;sup>a</sup> The filaments (Figure 3c, Figure 5, and Figure S7) contain 20 dimers.

#### DISCUSSION

The main finding of this work is that oligomers of I-BAR domains attain a curvature that is unrelated, in fact nearly orthogonal, to the intrinsic curvature of the dimer along its principal axis. The curved oligomer exposes a convex membrane binding surface and is thus consistent with generating negative membrane curvature. Both lateral and end-to-end interactions contribute to oligomerization, but the former are stronger. The relevant curvature develops along these lateral interactions. As a control, an F-BAR domain oligomer develops curvature in the opposite direction, consistent with positive membrane curvature generation. Binding energy calculations show that oligomerization increases the curvature sensitivity of the I-BAR domains.

Experimental evidence on I-BAR oligomerization is scarce. Slow fluorescence recovery in the absence of stiffening of nanotubes coated with high density of ABBA I-BARs indicated possible oligomerization but with flexible linkages (Barooji et al., 2016). Similar results were obtained with other BAR domains (Zhao et al., 2013). Only a slight tendency for oligomerization of I-BAR domains has been observed in the aqueous phase (Prévost *et al.*, 2015). The fact that our oligomers are stable in water may be due to the brief duration of the simulations or, more likely, to an overestimation of the driving forces for protein adhesion by the implicit solvent model. However, even if the stability of the oligomers is overestimated, the qualitative trends regarding curvature should be valid.

What causes the different curving of I-BAR and F-BAR oligomers? Some F-BARs, such as FBP17 and CIP4 (Shimada et al., 2007) have enough intrinsic curvature as dimers to generate tubules by orienting perpendicular to the tube axis and the radius of the tubules they generate

matches their intrinsic curvature. For these, oligomerization is needed only to provide sufficient protein density. Others, such as Fcho2 (Henne et al., 2007) and the pacsins (Bai et al., 2012; Wang et al., 2009), have kinked "wings" that give them an S-shape when viewed from above, while I-BARs are straight. The binding interface between dimers is very different for the BAR domains we considered here (Fig. 8). I-BAR dimers are parallel to each other with a lateral shift; the contact interface is extensive and the salt bridges that drive oligomerization occur mostly in helix 3, which is the one farthest from the membrane. This likely causes the membrane binding surface to curve in a convex way. The Fcho2 F-BAR appears to oligomerize end-to-middle and the wings make salt bridges in helix 1, close to the membrane, which likely causes the membrane binding surface to curve in a concave way. These structures provide many opportunities for validation by mutagenesis or distance measurements via DEER or FRET.

**Figure 8. Comparison of I-BAR and F-BAR dimers of dimers.** (A) I-BAR (B) F-BAR. View from the top as they interact in the planar sheets of Fig. 4 and S5, respectively.

Strictly speaking, since our implicit membranes are rigid, what we have measured is curvature sensing, not curvature generation. However, these processes are thermodynamically linked. A curvature sensor will generate curvature if the protein density and the differential membrane binding energy are sufficient to overcome the cost of membrane deformation. We can verify this using our results together with elasticity theory (Helfrich, 1973). Consider a membrane of area A and N I-BAR dimers. We bend the membrane into tubes of radius R and length L (A=2πRL). For large enough A we can neglect edge effects. If the percent surface coverage is φ and the area per dimer is  $\alpha$ , N/A =  $\varphi/\alpha$ . Based on the data in Table 2, the binding energy per dimer of filamentous oligomeric I-BAR to a membrane of radius R can be approximated as E<sub>b</sub> = -9.4 - 40nm/R kcal/mol down to R  $\sim 20$  nm. The energy of the tube relative to the flat membrane is E =  $\pi \kappa L/R + N$  (E<sub>b</sub>-E<sub>flat</sub>) or E/A =  $\kappa/2R^2 - \phi/\alpha$  40/R, where κ is the bending rigidity. The equilibrium radius is obtained by setting dE/dR = 0, giving  $R_{eq}$ = $\kappa\alpha/40\phi$ . For  $\kappa$ =12.5 kT(Prévost *et al.*, 2015),  $\alpha$ =50 nm²,  $\phi$ =0.25, and T=298 K we obtain  $R_{eq}$  = 37.5 nm. This is within the range of tubules observed experimentally (Mattila et al., 2007; Saarikangas et al., 2009). The balance between membrane deformation energy and protein binding leads to radii larger than the optimal 18 nm observed in preformed tubule experiments (Prévost et al., 2015) and the 13 nm curvature that the IRSp53 I-BAR oligomer develops spontaneously in our implicit water simulation. Clearly, the differential binding energies we calculate per dimer in the oligomeric state are sufficient for membrane curvature generation at reasonable surface densities.

In pulled tube experiments optimal partitioning is observed for 18-nm tubes (Prévost et al., 2015). Our binding energy calculations reproduce the stronger binding upon increasing the curvature to 20 nm and the reduction in binding from 20 nm to 10 nm at higher anionic fractions. At 30% anionic fraction, the binding affinity is about the same at 10 and 20 nm radius. The pulled tube experiments (Prévost et al., 2015) and another study (Barooji et al., 2016) found that the sorting ratio (partition coefficient) is higher at lower protein densities. This seems consistent with the formation of specific oligomeric structures in the tubule interiors with a definite, optimal protein density. As protein concentration increases, less optimal structures and curvatures are populated on the flat membrane and the sorting ratio decreases. The experiments showed that the sorting ratio was 20, 12 and 5 at overall protein area fraction 1%, 2%, and 5%, respectively. At these conditions, the surface coverage on the pulled tubes was 20, 24 and 25%, respectively. The surface area coverage of our spiral on Fig. 5 is ~ 8.2%, about 3 times lower, but it is feasible to construct tighter spirals with higher surface coverage. The sorting ratio calculated from our binding free energies of the individual dimer is 1.8, 2.7 and 6.4 in 30%, 50% and 75% anionic membranes, respectively (Table S3). For the oligomeric forms the sorting ratio is substantially higher. For example, for the 20-dimer oligomeric spiral in 50% anionic membrane it is ~25 (Table 2). Precise determination of the sorting ratio requires detailed consideration of oligomerization equilibria and determination of accurate oligomeric structures on both the flat membrane and the tube.

Previous MD simulations found that the IRSp53 domain flattens on the membrane and appears too flexible to support membrane remodeling based on its own intrinsic curvature (Takemura et al., 2017). This is consistent with our results. Another all-atom simulation with a single I-BAR dimer could not generate the expected high negative curvature, implying that some sort of oligomerization must play a role (Levtsova et al., 2011). Jarin et al. (Jarin et al., 2019) used two levels of coarse-graining to study the aggregation behavior of I-BAR dimers on membranes of various geometries. They found that I-BAR aggregates oriented parallel to the tube axis when the tube radius was narrow (25 nm) and perpendicular when the tube was wider (radius 50 nm). This is in agreement with our results. Another highly coarse-grained model observed side-by-side and end-to-end interactions which were controlled by the strength of the membrane-protein interaction, protein curvature and the inclusion of the PIP2 patches on the membrane(Jarin et al., 2021). These models employed purely repulsive protein-protein interactions and focused on membrane-mediated interactions. Thus, they could not predict oligomers of definite shape. Our results highlight the importance of protein-protein interactions and could be used to develop more realistic coarse-grained models that capture such effects and allow the study of detailed pathways of membrane deformation.

Several studies suggested that the lipid PI(4,5)P2 (PIP2) plays a role in I-BAR function (Mattila *et al.*, 2007; Saarikangas *et al.*, 2009). At neutral pH PIP2 has a charge of -4 (Brown, 2015) and its clustering by I-BAR (Saarikangas *et al.*, 2009) further increases the effective charge of the membrane and thus the binding energy. Theoretical treatments of anionic lipid segregation show that it increases membrane binding energy (Fleck *et al.*, 2002; Heimburg *et al.*, 1999; May *et al.*, 2000), essentially because the positively charged protein "feels" a higher effective negative charge on the membrane. In our implicit membrane model, which assumes uniform distribution of charge, we can take this into account in a "mean field" manner by using higher membrane anionic fractions than the nominal value. Considering this, the 50 or 70% anionic fractions where we observe the greatest curvature sensitivity are not unreasonable. In addition, Folch fraction I lipids commonly used in *in vitro* experiments (Wang *et al.*, 2009) have similar anionic fractions (Boura and Hurley, 2012).

Could the clustering of PIP2 or other anionic lipids be the *cause* of negative curvature generation? Several pieces of evidence argue against this. First, PIP2 is not strictly required for membrane remodeling (Barooji *et al.*, 2016; Chen et al., 2015) and the amount of clustering observed for other anionic lipids, such as PS, is much lower (Saarikangas *et al.*, 2009). Second, all BAR domains bind PIP2 and anionic lipids, but most generate positive curvature. Thus, the sign of curvature must be determined by something else. Even further, many proteins bind PIP2 but do not remodel membranes (Stuart McLaughlin et al., 2002). Third, a theory based on elasticity theory found that lipid demixing alone is not sufficient to bend the membrane in the case of the amphiphysin BAR domain (Khelashvili et al., 2009). Two coarse-grained studies found that IBAR domains can cluster PIP2-like lipids, but that was not accompanied by membrane deformation(Jarin *et al.*, 2021; Lin *et al.*, 2018);. Only if a curved membrane was preformed, could they see sorting of PIP2 into negative curvature regions (Lin *et al.*, 2018) or some effect of the protein-like inclusions on the shape of the protrusions(Jarin *et al.*, 2021). Based on the above, it seems to us unlikely that PIP2 clustering per se can account for negative curvature generation by IBARs.

In summary, our results suggest that the ability of IBAR domains to generate negative membrane curvature is due to the curvature of the oligomers they form and that in these oligomers the dimers are parallel to each other with a lateral shift. These predictions are testable by various experiments. Direct confirmation of the proposed oligomerization mode could perhaps be accomplished by AFM or EM on concave solid supported bilayers (Lee et al., 2015) of cylindrical shape. FRET or DEER after proper placement of labels would be another possibility for probing the structure of IBAR oligomers inside membrane tubules. A more indirect mutational approach would be to change the distribution of acidic and basic residues in a way that affects the predicted curvature of oligomers and measure the diameter of tubules generated. Salt bridges between ARG192 and GLU92 (3 Å), ASP181 and ARG84 (4 Å), GLU61 and LYS171 (5 Å), were detected on the oligomeric interface between the dimers and could be important for

oligomerization. However, it is also possible that the overall shape of the protein dictates the curvature of the oligomers more than specific interactions.

# **SUPPLEMENTAL INFORMATION**

Supplemental information can be found online at ...

# **ACKNOWLEDGMENTS**

This work was supported by the NIH (GM117146) and the NSF (MCB 1855942). Infrastructure support was provided in part by Research Centers in Minority Institutions grant no. 8G12MD007603 from the NIH. We thank the three anonymous reviewers for comments that led to substantial improvement of the article.

#### **AUTHOR CONTRIBUTIONS**

BN performed the bulk of the computations. AS contributed in the construction of the oligomers. BN and TL designed the research and wrote the manuscript.

#### **DECLARATION OF INTERESTS**

The authors declare no competing interests.

#### FIGURE CAPTIONS

- **Figure 1. Binding configuration of the dimer after 20 ns simulation.** (A) Flat membrane surface (B) Outside a spherical surface of radius 30 nm (C) Inside a spherical surface of radius 30 nm. The positively charged residues are shown in stick model. Shown is one of four independent trials, which give very similar results.  $\theta$  is the angle between the axes of the helices defined by residues 121-147.
- Figure 2. Configurations from self-assembly simulations of two or four I-BAR dimers on a flat membrane. (A) Initial configuration of two dimers. (B,C,D) Final configurations two dimers in different simulations. (E) Trimeric oligomer obtained from the free simulation of four dimers. Top view is shown in all figures.
- **Figure 3. Configurations of a chain of I-BAR dimers.** (A) Initial arrangement of a chain of dimers based on the crystal structure. (B) Final configuration obtained after simulation in implicit water. (C) Final configuration obtained from the simulation on a flat membrane surface (view from above).
- **Figure 4. Configurations of a sheet of I-BAR dimers.** (A) Initial structure of the planar sheet. (B,C) Final structure after simulation in implicit water, side view (B) and view along cylindrical axis (C).
- Figure 5. Final configuration of the pre-constructed spiral after 20 ns simulation in the interior of a 20-nm cylindrical tube. The initial and final pitch of the helix is 110 nm and 107 nm, respectively.
- Figure 6. Structure of tetramer of dimers obtained from the free simulation of multiple dimers on the flat membrane surface.

Figure 7. Linear filament designed by laterally overlapping two filaments with end-to-end interactions between the dimers. Figure 8. Comparison of I-BAR and F-BAR dimers of dimers. (A) I-BAR (B) F-BAR. View from the top as they interact in the planar sheets of Fig. 4 and S5, respectively.

# **TABLES**

Table 1. Binding energies of I-BAR dimer on cylindrical and spherical lipid membranes of different radius and anionic fraction. The curvature sensitivity parameter  $\alpha$  is determined from the data for radii 20 nm to 50 nm. Values in kcal/mol.

sphere						flat	α
	10nm	20nm	30nm	40nm	50nm	flat	
Inside (30%)	_a _	-7.2±0.3	-7.3±0.3	-7.2±0.2	-7.6±0.3		
Outside (30%	-4.8±0.4	-5.5±0.5	-6.4±0.5	-7.2±0.5	-6.8±0.6		
	cylinder						
	10nm	20nm	30nm	40nm	50nm		
Inside (30%)	-7.6±0.1	-7.6±0.4	-7.4±0.4	-7.3±0.5	-7.4±0.1	-7.3±0.5	0.4±0.2
Inside (50%)	-11.0±0.1	-11.2±0.4	-11.2±0.4	-10.8±0.1	-10.6±0.9	-10.6±0.1	1.2±0.4
Inside (75%)	-13.6±0.1	-14.1±0.5	-14.0±0.2	-13.6±0.4	-13.5±0.3	-13.0±0.5	1.3±0.2
Outside (30%)	-6.8±0.3	-7.3±0.3	-7.5±0.1	-7.2±0.2	-7.1±0.6		

a. The dimer is too long to fit inside a 10-nm sphere.

Table 2. Binding energy per dimer in a dimer of dimers and filamentous I-BAR on a 50% anionic membrane. Averages were calculated from three trials and the last 10 ns of a 20-ns simulation. Values in kcal/mol.

Radius	10nm	20nm	30nm	40nm	50nm	Flat	α	Sorting Ratio (S)
Dimer of dimers	-10.3±0.2	-10.3±0.3	-9.8±0.3	-9.5±0.2	-9.2±0.5	-9.0±0.3	2.0	6.6
Filame- ntous <sup>a</sup>		-11.3±0.2		-10.2±0.2		-9.4±0.2	1.63	25.0

<sup>&</sup>lt;sup>a</sup> The filaments (Figure 7, Figure 5, Figure S7) contain 20 dimers.

## STAR★ METHODS

## **KEY RESOURCES TABLE**

REAGENT or	SOURCE	IDENTIFIER
------------	--------	------------

RESOURCE							
Deposited data							
IRSp53 IBAR	(Millard et al., 2005)	1Y2O					
MIM IBAR	(Lee et al., 2007)	2D1L					
IBARa	(Linkner et al., 2014)	4NQI					
F-BAR	(Henne et al., 2007)	2V0O					
Software and algorithms							
CHARMM version 44a2	(Brooks et al., 2009)	https://www.charmm.org/					
VMD 1.9.4	(Humphrey et al., 1996)	https://www.ks.uiuc.edu/Research/vmd/					
PYMOL 2.3	(Schrodinger, 2015)	https://pymol.org/2/					

#### **RESOURCE AVAILABILITY**

#### Lead contact

Further information and requests for resources and reagents should be directed to and will be fulfilled by the Lead Contact, Themis Lazaridis (tlazaridis@ccny.cuny.edu).

## Materials availability

This study did not generate new unique materials.

## Data and code availability

The final coordinates of most simulations have been deposited to Zenodo (DOI 10.5281/zenodo.5068631). The parameters for initial coordinate generation are provided in Method Details.

This paper does not report original code.

Any additional information required to reanalyze the data reported in this paper is available from the lead contact upon request.

## **EXPERIMENTAL MODEL AND SUBJECT DETAILS**

No experimental models were used in this work. All data were obtained from computational methods using the CHARMM 44a2 program.

#### **METHOD DETAILS**

# Atomistic molecular dynamics simulations

The energy function used in the present work is an implicit membrane model for curved membranes (Nepal *et al.*, 2018). It is an extension of the IMM1 model for flat membranes (Lazaridis, 2003), which in turn is an extension of the implicit solvent energy function EEF1 for aqueous environments (Lazaridis and Karplus, 1999). The surface charge of the membrane is treated as uniform and calculated using the Gouy-Chapman theory in flat membranes (McLaughlin, 1989) or approximate analytical solutions to the Poisson-Boltzmann equation for

curved membranes (Nepal *et al.*, 2020). A more detailed description of the energy function and its applicability to the problem addressed here is given below.

The MD simulations were carried out with the EEF1 module of the CHARMM package (Brooks *et al.*, 2009). The simulations were run for 20 ns at 300 K with a 2-fs time step. Due to the lack of solvent friction, the true time-scale of implicit solvent simulations is much longer than their nominal duration. As a result, this duration was sufficient for achieving structural and energetic convergence (data available upon request). The trajectories were saved every 1 ps and analysis was done on the last 10 ns. The initial structure of the IRSp53 IBAR dimer was obtained from PDB code 1Y2O (Millard *et al.*, 2005). In the calculations, the width of the membrane hydrophobic core was set to 25.4 Å and the anionic fraction was set to 30%. For the higher oligomers, a 50% anionic membrane was used. The surface charge layer was set 3 Å outward from the hydrophobic-hydrophilic interface and 0.1 M salt concentration was used. Multiple trials were averaged to estimate statistical uncertainty.

The binding energies were estimated as average transfer energies, i.e. the difference in energy of the peptides on the membrane surface and the same conformation in bulk water. This is approximate, because it neglects possible changes in intramolecular energy (including such changes makes the results very noisy). Conformational and translational entropy is also neglected in these calculations, but these contributions are likely to be very similar in binding to flat and curved membranes. Two-sample t-tests were done to verify the statistical significance of binding energy differences for different curvatures (Table S4).

A quantitative measure of curvature sensitivity is the parameter  $\alpha$  defined by the equation(Nepal *et al.*, 2018)

 $\Delta \dot{G}^{\circ}$  = constant +  $\alpha \dot{x}$  RT  $\dot{x}$  In r (6) where r is the radius of the curvature.

# The Energy Function

The work presented herein was carried out using the implicit membrane model IMM1\_curv (Nepal et al., 2018), which is an extension to curved membranes of IMM1 (Lazaridis, 2003), which in turn is an extension to membranes of the implicit aqueous solvation model EEF1 (Effective Energy Function 1)(Lazaridis and Karplus, 1999). EEF1 is based on the united atom CHARMM force field(Neria et al., 1996), in which all atoms are represented explicitly except for the nonpolar hydrogens. A solvation free energy term is added that accounts for solvent exclusion due to neighboring atoms. The solvation term is calculated as the sum of group contributions:

$$\Delta G^{\text{slv}} = \sum_{i} \Delta G_{i}^{\text{slv}} = \sum_{i} \Delta G_{i}^{\text{ref}} - \sum_{i} \sum_{j \neq i} f_{i}(r_{ij}) V_{j}$$
where  $\Delta G_{i}^{\text{slv}}$  is the solvation free energy of atom i and  $\Delta G_{i}^{\text{ref}}$  is the solvation free energy of atom i

in a small model compound. The last term describes the loss of solvation free energy of atom I and  $\Delta G_i$  is the solvation free energy density of atom I calculated as a Gaussian function of  $r_{ij}$ ,  $r_{ij}$  is the distance between atoms i and j, and  $V_j$  is the volume of atom j. In addition to this term, a distance-dependent dielectric ( $\epsilon$ =r in Å) is used for Coulomb interactions. The titratable side chains do not carry a net charge but a partial charge distribution chosen to fit potentials of mean force between such side chains calculated in all-atom simulations(Masunov and Lazaridis, 2003). Interactions between the proteins in the aqueous phase, critical in this work, are governed by the common interatomic Lennard-Jones and screened Coulomb potentials and a desolvation term. Since its inception, EEF1 has been used extensively in applications such as protein structure prediction, design, and docking with Rosetta(Alford et al., 2017; Meiler and Baker, 2006; Rohl et al., 2004), peptide folding(Bottaro et al., 2013; Dinner et al., 1999) and unfolding(Best et al., 2003), NMR structure determination(Cavalli et al., 2007; Tian et al., 2014), studies of the protein denatured state(Lindorff-Larsen et al., 2004), analysis of contributions to protein stability(Ramos and Lazaridis, 2007; 2011) and binding affinity(Lazaridis et al., 2002), and many others.

In IMM1(Lazaridis, 2003) the membrane is treated as a hydrophobic slab and  $\Delta G_i^{ref}$  is modified to account for heterogeneous membrane-water systems:

 $\Delta G^{\text{ref}}(z') = f(z') \Delta G_i^{\text{ref, water}} + (1 - f(z')) \Delta G_i^{\text{ref; chex}}$ (8)

where  $\Delta G_i^{\text{ref,water}}$  and  $\Delta G_i^{\text{ref,chex}}$  are reference solvation free energies of atom i in water and cyclohexane, respectively. f(z') is a sigmoidal function that describes the vertical transition from one phase to the other:

$$f(z') = z'^{n}/1 + z'^{n},$$
 where  $z' = |z|/(T/2)$  (9)

where T is the thickness of the hydrophobic core of the membrane (typically 24-28 Å). The exponent n (usually n=10) controls the steepness of the transition. The increase in electrostatic interactions inside a membrane is taken into account by a modified dielectric screening function given by,

$$\varepsilon = r \int_{ij}^{ij} f_{ij} = \alpha + (1-\alpha) \sqrt{f_i f_j}$$
 (10)

where  $\alpha$  is an empirical parameter and was adjusted to 0.85 which gives membrane binding energies close to experiment. The surface charge due to anionic lipids is modeled based on the Gouy-Chapman theory, which is an analytical solution to the 1-d Poisson-Boltzmann equation assuming uniform charge on the membrane(Lazaridis, 2005). This plane of uniform charge (at the level of lipid phosphates) is typically placed 3 Å outward from the nonpolar-polar interface (f=0.5). The fraction of anionic lipids is set by the user. IMM1 has been applied to study membrane binding of peripheral proteins(Hajjar et al., 2008; Mihajlovic and Lazaridis, 2007; 2008; Prieto and Lazaridis, 2011), antimicrobial peptides(He and Lazaridis, 2013), membrane protein design(Alford et al., 2015; Barth et al., 2007; Joh et al., 2014), integral membrane proteins and assemblies(Donald et al., 2011; Favre et al., 2005; Strodel et al., 2010; Tang et al., 2006; Tian and Andricioaei, 2006), NMR structure refinement(Tian et al., 2015), GPCR drug discovery(Kortagere and Welsh, 2006) and others.

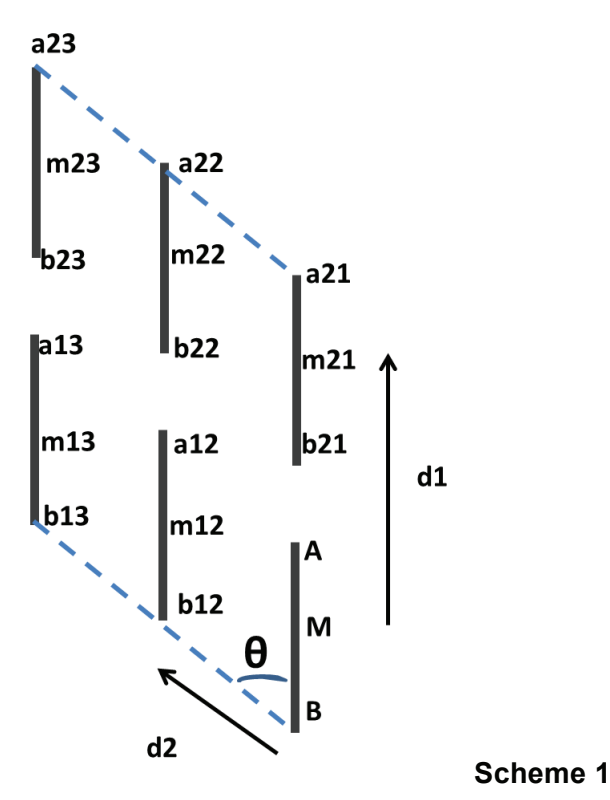
IMM1\_curv(Nepal *et al.*, 2018) modifies the shape of the hydrophobic region to account for a spherical (vesicle) or cylindrical (tube) shape. The center of the sphere is placed at the origin and R is the distance between the origin and the sphere mid-surface. The equation for z above is modified to z' = |r-R|/(T/2) where r is the distance of the atom from the origin, given by

$$r = \sqrt{x^2 + y^2 + z^2} \tag{11}$$

For a cylinder the x component is omitted, assuming that the cylindrical axis is along the x axis. The lateral pressure profile further takes account the lipid packing effect as a result of the curvature. Instead of the Gouy-Chapman model, which is appropriate for flat membranes, approximate analytical solutions to the nonlinear Poisson-Boltzmann equation were used to calculate the electrostatic interaction between the protein and the membrane surface charge with spherical and cylindrical shapes(Nepal *et al.*, 2020). The IMM1\_curv energy function includes an energy term for the lateral pressure profile, which is omitted in the present calculations because no insertion into the membrane interior takes place.

## Details of the construction of the oligomers

The sheets of the dimers were generated based on the scheme 1 below. AB and M represent the principal axis and the center of mass, respectively, of the initial I-BAR dimer, whereas aij, bij and mij are the corresponding properties of the replicas.  $\theta$  is the angle between the principal axis and the second replication axis and d1 and d2 are the respective translations vectors.



# 1. 1Y20 IBAR sheet (Fig 4)

The sheet was generated by replicating and translating the dimers along d1 and d2 with values 195 Å and 40 Å respectively. The angle  $\theta$  was 47.5°. The sheet had 60 dimers.

# 2. MIM-IBAR (PDB ID 2D1L) planar sheet (Fig S4a)

The sheet was generated by replicating and translating the dimers along d1 and d2 with values 193 Å and 41 Å respectively. The angle  $\theta$  was 43°. The sheet had 42 dimers.

## 3. IBARa (PDB ID 4NQI) planar sheet (Fig S5a)

The sheet was generated by replicating and translating the dimers along d1 and d2 with values 176 Å and 63 Å respectively. The angle  $\theta$  was 30°. The sheet had 42 dimers.

# 4. F-BAR (PDB ID 2V0O) planar sheet (Fig S6a)

The sheet was generated by replicating and translating the dimers along d1 and d2 with values 118 Å and 95 Å respectively. The angle  $\theta$  was 143°. The sheet had 20 dimers.

# 5. 20 nm helical spiral (Fig 5)

Dimers were replicated and translated along a helical spiral with radius 20 nm. The rotation angle of the helix was 35°. The separation distances between the dimers were maintained at 32 Å. The initial pitch length was 110 nm. The initial tilt angle of each dimer on the helical axis was 18°.

# 6. 40 nm helical spiral (Fig. S7)

Dimers were replicated and translated along a helical spiral with radius 40 nm. The rotation angle of the helix was 80°. The separation distances between the dimers were maintained at 32 Å. The initial pitch length was 110 nm. The initial tilt angle of each dimer on the helical axis was 85°.

## 7. End-to-end single chain helical spiral with radius 20 nm (Fig. S8)

The rotational angle of the helical spiral was 70°. The tilt angle of the dimer was also 70° so as to interact in the helical spiral end-to-end. The initial pitch length was 56 nm.

## 8. End-to-end double chain helical spiral with radius 20 nm (Fig. S9a)

The octameric unit in Fig. 6 was replicated along the helical spiral. The rotational angle for the spiral was 30°. The tilt angle of each dimer was 30° to the helical axis so as to interact end-to-end. The initial pitch length was 86 nm.

# 9. End-to-end double chain helical spiral with radius 40 nm (Fig. S9c)

The octameric unit in the Fig. 6 was replicated along the helical spiral. The rotational angle for the spiral was 40°. The tilt angle of each dimer was 40° to the helical axis so as to interact end-to-end. The initial pitch length was 168 nm.

#### 10. End-to-end double chain linear (Fig. 7)

The octameric unit in Fig 6 was replicated and translated along its long axis by 352 Å.

## **QUANTIFICATION AND STATISTICAL ANALYSIS**

For each radius, the average transfer energy was calculated from three identical simulations and the error was expressed as the standard deviation. The mean and standard deviations are presented in Tables 1 and 2. The curvature sensitivity parameter  $\alpha$  in Eq. (6) was obtained from the slope of the linear plot of  $\Delta G^{\circ}$  vs. radius r and the error was expressed as the standard error in the linear fitting. Two-sample t-tests were done to verify the statistical significance of binding energy differences for different curvatures (Table S4). No software was used.

## ADDITIONAL RESOURCES

No additional resources were generated by this study.

#### References

- Alford, R.F., Koehler Leman, J., Weitzner, B.D., Duran, A.M., Tilley, D.C., Elazar, A., and Gray, J.J. (2015). An Integrated Framework Advancing Membrane Protein Modeling and Design. PLOS Computational Biology *11*, e1004398. 10.1371/journal.pcbi.1004398.
- Alford, R.F., Leaver-Fay, A., Jeliazkov, J.R., O'Meara, M.J., DiMaio, F.P., Park, H., Shapovalov, M.V., Renfrew, P.D., Mulligan, V.K., Kappel, K., et al. (2017). The Rosetta All-Atom Energy Function for Macromolecular Modeling and Design. Journal of Chemical Theory and Computation *13*, 3031-3048. 10.1021/acs.jctc.7b00125.
- Bai, X., Meng, G., Luo, M., and Zheng, X. (2012). Rigidity of wedge loop in PACSIN 3 protein is a key factor in dictating diameters of tubules. J Biol Chem 287, 22387-22396. 10.1074/jbc.M112.358960.
- Barooji, Y.F., Rørvig-Lund, A., Semsey, S., Reihani, S.N.S., and Bendix, P.M. (2016). Dynamics of membrane nanotubes coated with I-BAR. Scientific Reports *6*, 30054. 10.1038/srep30054.

- Barth, P., Schonbrun, J., and Baker, D. (2007). Toward high-resolution prediction and design of transmembrane helical protein structures. Proceedings of the National Academy of Sciences 104, 15682-15687. 10.1073/pnas.0702515104.
- Best, R.B., Fowler, S.B., Toca Herrera, J.L., Steward, A., Paci, E., and Clarke, J. (2003). Mechanical Unfolding of a Titin Ig Domain: Structure of Transition State Revealed by Combining Atomic Force Microscopy, Protein Engineering and Molecular Dynamics Simulations. Journal of Molecular Biology 330, 867-877. https://doi.org/10.1016/S0022-2836(03)00618-1.
- Besterman, J.M., and Low, R.B. (1983). Endocytosis: a review of mechanisms and plasma membrane dynamics. Biochemical Journal *210*, 1-13.
- Bottaro, S., Lindorff-Larsen, K., and Best, R.B. (2013). Variational Optimization of an All-Atom Implicit Solvent Force Field To Match Explicit Solvent Simulation Data. Journal of Chemical Theory and Computation 9, 5641-5652. 10.1021/ct400730n.
- Boura, E., and Hurley, J.H. (2012). Structural basis for membrane targeting by the MVB12-associated β-prism domain of the human ESCRT-I MVB12 subunit. Proceedings of the National Academy of Sciences *109*, 1901-1906. 10.1073/pnas.1117597109.
- Breuer, A., Lauritsen, L., Bertseva, E., Vonkova, I., and Stamou, D. (2019). Quantitative investigation of negative membrane curvature sensing and generation by I-BARs in filopodia of living cells. Soft Matter *15*, 9829-9839. 10.1039/c9sm01185d.
- Brooks, B.R., Brooks III, C.L., Mackerell Jr., A.D., Nilsson, L., Petrella, R.J., Roux, B., Won, Y., Archontis, G., Bartels, C., Boresch, S., et al. (2009). CHARMM: The biomolecular simulation program. Journal of Computational Chemistry *30*, 1545-1614. 10.1002/jcc.21287.
- Brown, D.A. (2015). PIP2Clustering: From model membranes to cells. Chemistry and Physics of Lipids 192, 33-40. https://doi.org/10.1016/j.chemphyslip.2015.07.021.
- Cavalli, A., Salvatella, X., Dobson, C.M., and Vendruscolo, M. (2007). Protein structure determination from NMR chemical shifts. Proceedings of the National Academy of Sciences 104, 9615-9620. 10.1073/pnas.0610313104.
- Chen, Y.A., and Scheller, R.H. (2001). SNARE-mediated membrane fusion. Nature Reviews Molecular Cell Biology 2, 98. 10.1038/35052017.
- Chen, Z., Shi, Z., and Baumgart, T. (2015). Regulation of Membrane-Shape Transitions Induced by I-BAR Domains. Biophysical Journal *109*, 298-307. 10.1016/j.bpj.2015.06.010.
- Chernomordik, L.V., and Kozlov, M.M. (2008). Mechanics of membrane fusion. Nature Structural & Amp; Molecular Biology *15*, 675. 10.1038/nsmb.1455.
- Chlanda, P., Mekhedov, E., Waters, H., Sodt, A., Schwartz, C., Nair, V., Blank, P.S., and Zimmerberg, J. (2017). Palmitoylation Contributes to Membrane Curvature in Influenza A Virus Assembly and Hemagglutinin-Mediated Membrane Fusion. Journal of Virology *91*, UNSP e00947-17. 10.1128/jvi.00947-17.
- Dinner, A.R., Lazaridis, T., and Karplus, M. (1999). Understanding β-hairpin formation. Proceedings of the National Academy of Sciences *96*, 9068-9073. 10.1073/pnas.96.16.9068.
- Donald, J.E., Zhang, Y., Fiorin, G., Carnevale, V., Slochower, D.R., Gai, F., Klein, M.L., and DeGrado, W.F. (2011). Transmembrane orientation and possible role of the fusogenic peptide from parainfluenza virus 5 (PIV5) in promoting fusion. Proceedings of the National Academy of Sciences 108, 3958-3963. 10.1073/pnas.1019668108.
- Eitzen, G. (2003). Actin remodeling to facilitate membrane fusion. Biochimica et Biophysica Acta (BBA) Molecular Cell Research *1641*, 175-181. https://doi.org/10.1016/S0167-4889(03)00087-9.
- Favre, N., Fanelli, F., Missotten, M., Nichols, A., Wilson, J., di Tiani, M., Rommel, C., and Scheer, A. (2005). The DRY Motif as a Molecular Switch of the Human Oxytocin Receptor. Biochemistry 44, 9990-10008. 10.1021/bi0509853.
- Fleck, C., Netz, R.R., and von Grünberg, H.H. (2002). Poisson–Boltzmann Theory for Membranes with Mobile Charged Lipids and the pH-Dependent Interaction of a DNA Molecule with a Membrane. Biophysical Journal 82, 76-92. 10.1016/s0006-3495(02)75375-7.

- Frost, A., Perera, R., Roux, A., Spasov, K., Destaing, O., Egelman, E.H., De Camilli, P., and Unger, V.M. (2008). Structural Basis of Membrane Invagination by F-BAR Domains. Cell 132, 807-817. 10.1016/j.cell.2007.12.041.
- Graber, Z.T., Shi, Z., and Baumgart, T. (2017). Cations induce shape remodeling of negatively charged phospholipid membranes. Physical Chemistry Chemical Physics *19*, 15285-15295. 10.1039/c7cp00718c.
- Hajjar, E., Mihajlovic, M., Witko-Sarsat, V., Lazaridis, T., and Reuter, N. (2008). Computational prediction of the binding site of proteinase 3 to the plasma membrane. Proteins: Structure, Function, and Bioinformatics *71*, 1655-1669. https://doi.org/10.1002/prot.21853.
- He, Y., and Lazaridis, T. (2013). Activity Determinants of Helical Antimicrobial Peptides: A Large-Scale Computational Study. PLOS ONE *8*, e66440. 10.1371/journal.pone.0066440.
- Heimburg, T., Angerstein, B., and Marsh, D. (1999). Binding of Peripheral Proteins to Mixed Lipid Membranes: Effect of Lipid Demixing upon Binding. Biophysical Journal 76, 2575-2586. https://doi.org/10.1016/S0006-3495(99)77410-2.
- Helfrich, W. (1973). Elastic properties of lipid bilayers: theory and possible experiments. Z Naturforsch C 28, 693-703. 10.1515/znc-1973-11-1209.
- Henne, W.M., Kent, H.M., Ford, M.G.J., Hegde, B.G., Daumke, O., Butler, P.J.G., Mittal, R., Langen, R., Evans, P.R., and McMahon, H.T. (2007). Structure and Analysis of FCHo2 F-BAR Domain: A Dimerizing and Membrane Recruitment Module that Effects Membrane Curvature. Structure 15, 839-852. 10.1016/j.str.2007.05.002.
- Humphrey, W., Dalke, A., and Schulten, K. (1996). VMD: Visual molecular dynamics. Journal of Molecular Graphics *14*, 33-38. https://doi.org/10.1016/0263-7855(96)00018-5.
- Jarin, Z., Pak, A.J., Bassereau, P., and Voth, G.A. (2021). Lipid-Composition-Mediated Forces Can Stabilize Tubular Assemblies of I-BAR Proteins. Biophysical Journal *120*, 46-54. https://doi.org/10.1016/j.bpj.2020.11.019.
- Jarin, Z., Tsai, F.-C., Davtyan, A., Pak, A.J., Bassereau, P., and Voth, G.A. (2019). Unusual Organization of I-BAR Proteins on Tubular and Vesicular Membranes. Biophysical Journal 117, 553-562. https://doi.org/10.1016/j.bpj.2019.06.025.
- Joh, N.H., Wang, T., Bhate, M.P., Acharya, R., Wu, Y., Grabe, M., Hong, M., Grigoryan, G., and DeGrado, W.F. (2014). De novo design of a transmembrane Zn<sup>2+</sup>-transporting four-helix bundle. Science *346*, 1520-1524. 10.1126/science.1261172.
- Kaksonen, M., and Roux, A. (2018). Mechanisms of clathrin-mediated endocytosis. Nature Reviews Molecular Cell Biology 19, 313. 10.1038/nrm.2017.132.
- Khelashvili, G., Harries, D., and Weinstein, H. (2009). Modeling Membrane Deformations and Lipid Demixing upon Protein-Membrane Interaction: The BAR Dimer Adsorption. Biophysical Journal *97*, 1626-1635. 10.1016/j.bpj.2009.07.006.
- Kortagere, S., and Welsh, W.J. (2006). Development and application of hybrid structure based method for efficient screening of ligands binding to G-protein coupled receptors. Journal of Computer-Aided Molecular Design 20, 789-802. 10.1007/s10822-006-9077-8.
- Lazaridis, T. (2003). Effective energy function for proteins in lipid membranes. Proteins: Structure, Function, and Bioinformatics *52*, 176-192. 10.1002/prot.10410.
- Lazaridis, T. (2005). Implicit solvent simulations of peptide interactions with anionic lipid membranes. Proteins: Structure, Function, and Bioinformatics 58, 518-527. https://doi.org/10.1002/prot.20358.
- Lazaridis, T., and Karplus, M. (1999). Effective energy function for proteins in solution. Proteins: Structure, Function, and Bioinformatics 35, 133-152. 10.1002/(sici)1097-0134(19990501)35:2<133::aid-prot1>3.0.co;2-n.
- Lazaridis, T., Masunov, A., and Gandolfo, F. (2002). Contributions to the binding free energy of ligands to avidin and streptavidin. Proteins: Structure, Function, and Bioinformatics 47, 194-208. https://doi.org/10.1002/prot.10086.
- Lee, I.-H., Kai, H., Carlson, L.-A., Groves, J.T., and Hurley, J.H. (2015). Negative membrane curvature catalyzes nucleation of endosomal sorting complex required for transport (ESCRT)-III assembly. Proceedings of the National Academy of Sciences *112*, 15892-15897. 10.1073/pnas.1518765113.

- Lee, S.H., Kerff, F., Chereau, D., Ferron, F., Klug, A., and Dominguez, R. (2007). Structural Basis for the Actin-Binding Function of Missing-in-Metastasis. Structure *15*, 145-155. 10.1016/j.str.2006.12.005.
- Levtsova, O.V., Davletov, I.D., Sokolova, O.S., and Shaitan, K.V. (2011). A molecular dynamics study of the interaction between domain I-BAR of the IRSp53 protein and negatively charged membranes. Biophysics *56*, 220-224. 10.1134/s0006350911020199.
- Lin, X., Wang, H., Lou, Z., Cao, M., Zhang, Z., and Gu, N. (2018). Roles of PIP2 in the membrane binding of MIM I-BAR: insights from molecular dynamics simulations. FEBS Letters *592*, 2533-2542. 10.1002/1873-3468.13186.
- Lindorff-Larsen, K., Kristjansdottir, S., Teilum, K., Fieber, W., Dobson, C.M., Poulsen, F.M., and Vendruscolo, M. (2004). Determination of an Ensemble of Structures Representing the Denatured State of the Bovine Acyl-Coenzyme A Binding Protein. Journal of the American Chemical Society *126*, 3291-3299. 10.1021/ja039250g.
- Linkner, J., Witte, G., Zhao, H., Junemann, A., Nordholz, B., Runge-Wollmann, P., Lappalainen, P., and Faix, J. (2014). The inverse BAR domain protein IBARa drives membrane remodeling to control osmoregulation, phagocytosis and cytokinesis. Journal of Cell Science 127, 1279-1292. 10.1242/jcs.140756.
- Masuda, M., Takeda, S., Sone, M., Ohki, T., Mori, H., Kamioka, Y., and Mochizuki, N. (2006). Endophilin BAR domain drives membrane curvature by two newly identified structure-based mechanisms. The EMBO Journal *25*, 2889-2897. 10.1038/sj.emboj.7601176.
- Masunov, A., and Lazaridis, T. (2003). Potentials of Mean Force between Ionizable Amino Acid Side Chains in Water. Journal of the American Chemical Society *125*, 1722-1730. 10.1021/ja025521w.
- Mattila, P.K., Pykäläinen, A., Saarikangas, J., Paavilainen, V.O., Vihinen, H., Jokitalo, E., and Lappalainen, P. (2007). Missing-in-metastasis and IRSp53 deform PI(4,5)P2-rich membranes by an inverse BAR domain–like mechanism. Journal of Cell Biology *176*, 953-964. 10.1083/jcb.200609176.
- May, S., Harries, D., and Ben-Shaul, A. (2000). Lipid Demixing and Protein-Protein Interactions in the Adsorption of Charged Proteins on Mixed Membranes. Biophysical Journal 79, 1747-1760. 10.1016/s0006-3495(00)76427-7.
- McLaughlin, S. (1989). The Electrostatic Properties of Membranes. Annual Review of Biophysics and Biophysical Chemistry 18, 113-136. 10.1146/annurev.bb.18.060189.000553.
- Meiler, J., and Baker, D. (2006). ROSETTALIGAND: Protein–small molecule docking with full side-chain flexibility. Proteins: Structure, Function, and Bioinformatics 65, 538-548. https://doi.org/10.1002/prot.21086.
- Mihajlovic, M., and Lazaridis, T. (2007). Modeling fatty acid delivery from intestinal fatty acid binding protein to a membrane. Protein Science 16, 2042-2055. https://doi.org/10.1110/ps.072875307.
- Mihajlovic, M., and Lazaridis, T. (2008). Membrane-bound structure and energetics of  $\alpha$ -synuclein. Proteins: Structure, Function, and Bioinformatics 70, 761-778. https://doi.org/10.1002/prot.21558.
- Millard, T.H., Bompard, G., Heung, M.Y., Dafforn, T.R., Scott, D.J., Machesky, L.M., and Fütterer, K. (2005). Structural basis of filopodia formation induced by the IRSp53/MIM homology domain of human IRSp53. The EMBO Journal *24*, 240-250. 10.1038/sj.emboj.7600535.
- Nepal, B., Leveritt, J., and Lazaridis, T. (2018). Membrane Curvature Sensing by Amphipathic Helices: Insights from Implicit Membrane Modeling. Biophysical Journal *114*, 2128-2141. https://doi.org/10.1016/j.bpj.2018.03.030.
- Nepal, B., Sepehri, A., and Lazaridis, T. (2020). Mechanisms of negative membrane curvature sensing and generation by ESCRT III subunit Snf7. Protein Science 29, 1473-1485. 10.1002/pro.3851.
- Neria, E., Fischer, S., and Karplus, M. (1996). Simulation of activation free energies in molecular systems. The Journal of Chemical Physics *105*, 1902-1921. 10.1063/1.472061.
- Pang, X., Fan, J., Zhang, Y., Zhang, K., Gao, B., Ma, J., Li, J., Deng, Y., Zhou, Q., Egelman, Edward H., et al. (2014). A PH Domain in ACAP1 Possesses Key Features of the BAR

- Domain in Promoting Membrane Curvature. Developmental Cell *31*, 73-86. 10.1016/j.devcel.2014.08.020.
- Peter, B.J., Kent, H.M., Mills, I.G., Vallis, Y., Butler, P.J.G., Evans, P.R., and McMahon, H.T. (2004). BAR Domains as Sensors of Membrane Curvature: The Amphiphysin BAR Structure. Science 303, 495-499. 10.1126/science.1092586.
- Prévost, C., Zhao, H., Manzi, J., Lemichez, E., Lappalainen, P., Callan-Jones, A., and Bassereau, P. (2015). IRSp53 senses negative membrane curvature and phase separates along membrane tubules. Nature Communications *6*, 8529. 10.1038/ncomms9529.
- Prieto, L., and Lazaridis, T. (2011). Computational studies of colicin insertion into membranes: The closed state. Proteins: Structure, Function, and Bioinformatics 79, 126-141. https://doi.org/10.1002/prot.22866.
- Ramos, J., and Lazaridis, T. (2007). Energetic Determinants of Oligomeric State Specificity in Coiled Coils [J. Am. Chem. Soc. 2006, 128, 15499–15510]. Journal of the American Chemical Society 129, 3455-3456. 10.1021/ja076882k.
- Ramos, J., and Lazaridis, T. (2011). Computational analysis of residue contributions to coiled-coil topology. Protein Science *20*, 1845-1855. https://doi.org/10.1002/pro.718.
- Rohl, C.A., Strauss, C.E.M., Misura, K.M.S., and Baker, D. (2004). Protein Structure Prediction Using Rosetta. In Methods in Enzymology, (Academic Press), pp. 66-93. https://doi.org/10.1016/S0076-6879(04)83004-0.
- Saarikangas, J., Zhao, H., and Lappalainen, P. (2010). Regulation of the Actin Cytoskeleton-Plasma Membrane Interplay by Phosphoinositides. Physiological Reviews *90*, 259-289. 10.1152/physrev.00036.2009.
- Saarikangas, J., Zhao, H., Pykäläinen, A., Laurinmäki, P., Mattila, P.K., Kinnunen, P.K.J., Butcher, S.J., and Lappalainen, P. (2009). Molecular Mechanisms of Membrane Deformation by I-BAR Domain Proteins. Current Biology *19*, 95-107. https://doi.org/10.1016/j.cub.2008.12.029.
- Schrodinger, LLC (2015). The PyMOL Molecular Graphics System, Version 1.8.
- Shimada, A., Niwa, H., Tsujita, K., Suetsugu, S., Nitta, K., Hanawa-Suetsugu, K., Akasaka, R., Nishino, Y., Toyama, M., Chen, L., et al. (2007). Curved EFC/F-BAR-Domain Dimers Are Joined End to End into a Filament for Membrane Invagination in Endocytosis. Cell *129*, 761-772. https://doi.org/10.1016/j.cell.2007.03.040.
- Shukla, S., Jin, R., Robustelli, J., Zimmerman, Z.E., and Baumgart, T. (2019). PIP2 Reshapes Membranes through Asymmetric Desorption. Biophysical Journal 117, 962-974. https://doi.org/10.1016/j.bpj.2019.07.047.
- Strodel, B., Lee, J.W.L., Whittleston, C.S., and Wales, D.J. (2010). Transmembrane Structures for Alzheimer's A $\beta$ 1–42 Oligomers. Journal of the American Chemical Society *132*, 13300-13312. 10.1021/ja103725c.
- Stuart McLaughlin, Jiyao Wang, Alok Gambhir, and Murray, D. (2002). PIP2 and Proteins: Interactions, Organization, and Information Flow. Annual Review of Biophysics and Biomolecular Structure *31*, 151-175. 10.1146/annurev.biophys.31.082901.134259.
- Suetsugu, S. (2010). The proposed functions of membrane curvatures mediated by the BAR domain superfamily proteins. The Journal of Biochemistry *148*, 1-12. 10.1093/jb/mvq049.
- Suetsugu, S., Murayama, K., Sakamoto, A., Hanawa-Suetsugu, K., Seto, A., Oikawa, T., Mishima, C., Shirouzu, M., Takenawa, T., and Yokoyama, S. (2006). The RAC Binding Domain/IRSp53-MIM Homology Domain of IRSp53 Induces RAC-dependent Membrane Deformation \*. Journal of Biological Chemistry 281, 35347-35358. 10.1074/jbc.M606814200.
- Takemura, K., Hanawa-Suetsugu, K., Suetsugu, S., and Kitao, A. (2017). Salt Bridge Formation between the I-BAR Domain and Lipids Increases Lipid Density and Membrane Curvature. Scientific Reports 7, 6808. 10.1038/s41598-017-06334-5.
- Tang, Y., Cao, G., Chen, X., Yoo, J., Yethiraj, A., and Cui, Q. (2006). A Finite Element Framework for Studying the Mechanical Response of Macromolecules: Application to the Gating of the Mechanosensitive Channel MscL. Biophysical Journal *91*, 1248-1263. 10.1529/biophysj.106.085985.

- Tian, P., and Andricioaei, I. (2006). Size, Motion, and Function of the SecY Translocon Revealed by Molecular Dynamics Simulations with Virtual Probes. Biophysical Journal *90*, 2718-2730. https://doi.org/10.1529/biophysj.105.073304.
- Tian, Y., Schwieters, C.D., Opella, S.J., and Marassi, F.M. (2014). A practical implicit solvent potential for NMR structure calculation. Journal of Magnetic Resonance *243*, 54-64. https://doi.org/10.1016/j.jmr.2014.03.011.
- Tian, Y., Schwieters, Charles D., Opella, Stanley J., and Marassi, Francesca M. (2015). A Practical Implicit Membrane Potential for NMR Structure Calculations of Membrane Proteins. Biophysical Journal *109*, 574-585. 10.1016/j.bpj.2015.06.047.
- Wang, Q., Navarro, M.V.A.S., Peng, G., Molinelli, E., Lin Goh, S., Judson, B.L., Rajashankar, K.R., and Sondermann, H. (2009). Molecular mechanism of membrane constriction and tubulation mediated by the F-BAR protein Pacsin/Syndapin. Proceedings of the National Academy of Sciences *106*, 12700-12705. 10.1073/pnas.0902974106.
- Wu, L.-G., Hamid, E., Shin, W., and Chiang, H.-C. (2014). Exocytosis and Endocytosis: Modes, Functions, and Coupling Mechanisms. Annual Review of Physiology *76*, 301-331. 10.1146/annurev-physiol-021113-170305.
- Zhao, H., Michelot, A., Koskela, E.V., Tkach, V., Stamou, D., Drubin, D.G., and Lappalainen, P. (2013). Membrane-sculpting BAR domains generate stable lipid microdomains. Cell Reports *4*, 1213-1223. 10.1016/j.celrep.2013.08.024.
- Zhu, G., Chen, J., Liu, J., Brunzelle, J.S., Huang, B., Wakeham, N., Terzyan, S., Li, X., Rao, Z., Li, G., and Zhang, X.C. (2007). Structure of the APPL1 BAR-PH domain and characterization of its interaction with Rab5. The EMBO Journal *26*, 3484-3493. 10.1038/sj.emboj.7601771.